Journal of Membrane Science 687 (2023) 122071

Contents lists available at ScienceDirect

Journal of Membrane Science

journal homepage: www.elsevier.com/locate/memsci

Tailoring highly stable anion exchange membranes with graft molecular structure ordering using reversible addition-fragmentation chain transfer polymerization for alkaline fuel cells

Bianca Pedroso S. Santos [a,**], Andrey S. Barbosa [a], Yasko Kodama [a], Thiago B. de Queiroz [b], Elisabete I. Santiago [a,*]

[a] Nuclear and Energy Research Institute, IPEN/CNEN, 05508-000, São Paulo, Brazil
[b] Center for Natural and Human Sciences, Federal University of ABC, 09210-580, Santo André, Brazil

ARTICLE INFO

Keywords:
Anion-exchange membranes
ETFE
Radiation-induced grafting
RAFT
AEMFC

ABSTRACT

The radiation-induced grafting is used to prepare a variety of anion-exchange membranes (AEM) based on poly (ethylene-*co*-tetrafluoroethylene) (ETFE) utilizing a reversible addition-fragmentation chain transfer (RAFT) agent. The copolymerization process is controlled by the RAFT agent, resulting in AEMs with a restricted molecular weight dispersion. As a result, RAFT-AEMs exhibit decreased water uptake and reduced swelling. A significant improvement in thermal and mechanical characteristics is evidenced, while the conductivity remains practically unaltered. Anion-exchange membrane fuel cell (AEMFC) tests revealed that conventional RIG-AEMs and RAFT-AEMs with low RAFT content (5 wt%) have comparable beginning-of-life performances (~0.95 W cm^{-2}). However, for higher RAFT contents, the performance trends to decrease indicating an imbalance in water management. Furthermore, short-term stability tests suggest that RAFT-AEMs are able to operate highly stable, with a conductivity rate loss of 0.05% h^{-1}, which represents an improvement of 160% in comparison to conventional RIG-AEM. AFM analysis demonstrated that structural ordering molecular and morphology tailor the fundamental properties of ETFE-based AEMs, combining enhanced performance and stability for alkaline fuel cell applications.

1. Introduction

Anion exchange membrane fuel cells (AEMFC) constitute the new generation of alkaline fuel cells, whose main feature is the replacement of liquid electrolytes with polymeric anion-exchange membranes. AEMFCs have many benefits and advantages over other types of fuel cells, such as reduced fuel crossover and fast cathode reaction kinetics in alkaline medium. This feature proposes the AEMFCs as a more economically viable alternative to the well-established proton-exchange membrane fuel cells (PEMFCs) due to the possibility of using abundant catalysts, e.g., non-Platinum Group Metal (non-PGM) [1–3].

Anion exchange membranes (AEM) are ionomeric materials composed of non-ionic (polymer backbone) and ionic phases (functionalized copolymer), which allow to membrane the ability to anion conduction [4,5]. In general, the polymer backbone ensures the chemical and mechanical properties to AEM, while functional groups covalently bonded to side chains are responsible for the ionic conduction process [6]. Thus, AEM is the key component of new-generation clean-energy conversion devices such as fuel cells, electrolyzers, batteries, and electrodialyzers to mitigate environmental pollution [7–10].

To obtain high-performance AEMs, the candidates should exhibit high anion conductivity and maintain mechanical integrity and chemical stability for different application purposes. The methods used to obtain these properties involve the optimization of synthesis strategies, the development of more stable functional groups, and the use of polymeric matrices with increased mechanical and chemical stabilities [11]. One of the most employed methods for AEM synthesis is radiation-induced grafting (RIG). The RIG is an interesting strategy because it can be applied in pre-formed commercial polymers, allowing the control of the degree of monomer copolymerized by changing the synthesis parameters without a need for a catalyst or another type of polymerization initiators, preventing further purification steps [12,13].

* Corresponding author.
** Corresponding author.
E-mail addresses: bianca.pedroso3@gmail.com (B.P.S. Santos), elisabete.santiago@usp.br (E.I. Santiago).

https://doi.org/10.1016/j.memsci.2023.122071
Received 7 April 2023; Received in revised form 16 August 2023; Accepted 6 September 2023
Available online 7 September 2023

This approach can be used in several types of polymers and monomers, and it is considered an easy, relatively cheap, and efficient method for AEM production [14]. On the other hand, controlling and tailoring structural properties such as molecular weight and dispersion of grafted polymers are not achieved using RIG methods [15]. In addition, the occurrence of parallel reactions, mainly chain scission, and crosslinking during RIG can lead to modification in the polymeric structure, affecting its chemical and mechanical properties.

The reversible deactivation radical polymerization (RDRP) methodology has challenged the field of polymer synthesis due to the possibility of producing polymers with controlled dispersity and molecular architecture such as multi-block, star, graft, alternating sequences, and other functionalities, which are not possible in the conventional free-radical polymerization (FRP) [16–18]. Among the methods of RDRP, the most common strategies are atom transfer radical polymerization (ATRP), nitroxide-mediated polymerization (NMP), and reversible addition-fragmentation chain transfer polymerization (RAFT). The NMP technique demands a long time and high temperature for the polymerization process to occur, in addition, a reduced number of monomer types can be employed, whereas ATRP is generally a costly process due to the necessity of catalyst removal. Hence, RAFT polymerization has significant advantages over other RDRP techniques, which consist of the possibility of using many types of monomers and solvents under mild reaction conditions. This method can be adaptable to different systems of reaction initiation (UV-induced or gamma-induced) and promotes a more homogeneous grafting than conventional FRP as RIG method [19–21].

In general, molecular structure control in RAFT-based synthesized materials is usually achieved by using a chain transfer agent (CTA). The most used CTA is a dithioester-derivative, which has a strong ability to control molecular growth. Therefore, the synthesis mechanism is similar to conventional radical polymerization, but the main difference is the polymerization control obtained by the interchange of polymer radicals and organosulfur-based chain-transfer agents [22–25]. Although RAFT methodology has been requested in the control of the molecular weight of copolymerization processes, the mechanism understanding, polymer synthesis, and applications of RAFT-based materials are still scarce [26–29].

Polymer backbones are commonly used in the preparation of RIG-AEM due to the rapid formation of active sites for a suitable polymer matrix accomplishment [14]. Among the preferred backbones for AEMs, poly(ethylene-*co*-tetrafluoroethylene) (ETFE) occupies a special position for combining hydrocarbon and fluorocarbon segments, which in turn leads to enhanced properties, such as good chemical, thermal and mechanical stability, besides high susceptibility of producing a large number of free radicals for grafting reaction [30–32]. Thus, these were the reasons for the choice of ETFE as the polymer matrix used to advance in strategies of synthesis of AEMs with rigorous molecular structure control in this exploratory study.

The present work proposes the synthesis of a radiation-induced grafted ETFE-based high-stability anion-exchange membrane with a well-ordered molecular structure via the RAFT polymerization technique. Herein, properties of RAFT-based AEMs as thermal, chemical, morphological, mechanical, and electrical properties were extensively explored. Also, the resulting AEMs were evaluated in terms of performance and stability, proving to be promising candidates as electrolytes for AEMFC devices.

2. Experimental

2.1. Materials

Poly(ethylene-*co*-tetrafluoroethylene) film (25 μm, Nowofol) was used as pre-formed commercial polymer. Analytical grade chemicals and reagents were used as received. The following reagents were purchased from Sigma-Aldrich: cyanomethyl dodecyl trithiocarbonate (RAFT agent), trimethylamine (TMA, 45% vol.), α-alumina, potassium hydroxide, acetone, toluene and $CDCl_3$ deuterated (NMR grade). The mixture of isomers 3- and 4-vinylbenzyl chloride (VBC, 96%), employed as monomer, was supplied by Polysciences Chemistry Company. The inhibitor of VBC was removed using a column with α-alumina.

2.2. Synthesis of AEMs

2.2.1. Grafting step

The grafting was performed by simultaneous method, which consists of irradiating concomitantly both base polymer and monomer. Conventional radiation-induced grafted AEMs were prepared taking place ETFE films (18 × 3 cm) immersed in a mixture with inhibitor-free VBC (1.25 mL) and acetone (2.95 mL), in hermetically sealed vials. This sample will be referred as E0 to grafted-ETFE obtained by conventional RIG method. For RAFT-based membrane synthesis, different contents of RAFT agent, 5 mg, 15 mg and 30 mg were added. Such membranes were named E5, E15, and E30, respectively. Set of vials was irradiated with γ-rays from ^{60}Co sources (Gamma Cell 220 - Atomic Energy of Canada Limited) with radiation absorbed dose of 15 kGy, activity of 17 TBq, and dose rate of 396.59 Gy h^{-1} during 37.82 h at room temperature (RT, ~25 °C). The radiation dose was fixed at 15 kGy aiming to evaluate the RAFT agent effect in the grafting process as well as minimize the impairment of the mechanical properties of the ETFE film due to chain scission degradation by γ-radiation at RT. The obtained grafted-ETFE was exhaustively washed with toluene and acetone to remove residual monomers and homopolymer. Finally, the grafted membranes (ETFE-g-poly(VBC)) were dried in a vacuum oven for 12 h.

2.2.2. Amination step

The amination reaction refers to the introduction of quaternary ammonium (QA) groups and was carried out by immersion of ETFE-g-poly(VBC) films into a TMA solution (45% vol.) under constant stirring at RT for 24 h. As a sequence, ETFE-g-poly(VBC)-TMA membranes were exhaustively washed with ultrapure water (UPW) following heat wash for 2 h to remove the residual TMA.

2.2.3. ETFE-g-poly(VBC)-TMA in the chloride form

To avoid inaccurate data resulting from the carbonation process by ambient CO_2, the ETFE-g-poly(VBC)-TMA was conditioned in the chloride form. AEMs in the chloride form were obtained by immersion in an aqueous solution of NaCl (1 M) at RT for 24 h accompanied by three replacements with fresh solution during this period. The AEMs were subsequently washed thoroughly with UPW to remove residual excess of NaCl and stored in UPW until their use.

2.3. AEMs characterizations

2.3.1. The chemical structure analysis and molecular weight measurement

In order to study the chemical structure and molecular weight distribution of the AEMs as a function of the RAFT agent content, ^{13}C solid-state nuclear magnetic resonance (NMR) spectroscopy, Raman spectroscopy, and gel permeation chromatography (GPC) analysis were performed.

NMR experiments were conducted in a Varian VNMRS 500 MHz spectrometer operating at the ^{13}C resonance frequency of 125.7 MHz. For solid-state measurements, $^{13}C\{^1H\}$ cross-polarization, (CP) NMR experiments were obtained for membranes at magic angle spinning (MAS) of 6, 8 and 10 kHz with a contact time of 0.5 μs, relaxation delay of 5 s, ^{1}H-π/2 pulse length of 2.5 μs, and ^{1}H TPPM decoupling [33]. Typically, ~1400 transients were collected. The FIDs Fourier transform was weighted by a line-broadening factor of 100 Hz. Since in the CP, the magnetization transfer is unfavored at higher MAS rates, the experiments at MAS of 6 kHz were chosen to be discussed. Chemical shifts are reported relative to tetramethylsilane (TMS) at 0 ppm for ^{1}H and ^{13}C, using adamantine as a secondary reference for the ^{13}C with the CH_2

carbon at 38.5 ppm. The spectra were deconvoluted using Gaussian/-Lorentzian distributions with the DMFit software [34].

Raman spectra were obtained from a Horiba Jobin Yvon, model XploRA-PLUS spectrometer with a laser wavelength 785 nm, power of 85 mW, objective lens of 50X, numerical aperture (NA) of 0.50 N A., HORIBA Instruments Incorporated/Syncerity TM CCD detector and a resolution of 4 cm^{-1} using the software LabSpec6.

GPC was carried out to determine the molecular weight and dispersion of the remaining grafting solution after the irradiation step and membrane removal. The Prominence UFLC Shimadzu system was equipped with two Columns: the first Waters Sytragel pre-column, 4.6 × 30 mm, 500 Å and the second Phenogel 5 μm Linear (2), 7.8 mm × 300 mm (2x) and calibrated with poly(styrene) standards (100–1x10^7 Da) in chromatographic grade $CHCl_3$.

2.4. Thermal properties characterizations

Thermogravimetric analysis (TGA) was carried out using TG/DTA/SDT Q600 model, TA Instruments with a heating rate of 10 °C min^{-1} in a temperature range of 25–650 °C under N_2 atmosphere at 100 mL min^{-1}. The differential scanning calorimetry (DSC) measurements were performed in the equipment Perkin Elmer model DSC6000 to measure the melting and crystallization temperatures. Samples (~5 mg) were sealed in aluminum pans, and the experiments were carried out by heating-cooling-heating with the rate of 10 °C min^{-1} from room temperature up to 300 °C under N_2 atmosphere flow of 50 mL min^{-1}.

2.5. Mechanical characterization

The mechanical properties of membranes (Young's modulus (MPa), tensile strength (%), and elongation at break (%) were measured at room temperature using a universal test machine, Instron model 5567, cell load 1 kN. Long-strip specimens were die-cut with a width of 4 mm and a length of 25 mm. Employing the same test protocol, three specimens of each sample were tested to minimize errors associated with measurements.

2.6. Degree of grafting (DoG), ion exchange capacity (IEC), gravimetric water uptake (WU), through-plane swelling (TPS), in-plane swelling (IPS), hydration number (λ)

The degree of grafting (DoG) of grafted samples was estimated by gravimetry based on the difference in ETFE-g-poly(VBC) film weights before and after the grafting step as shown in Equation 1 (Table 1). IEC measurements were carried out in a Titrino 848 Plus titrator (Metrohm) using an electrode of Ag/AgCl. Dry ETFE-g-poly(VBC)-AEMs in chloride form were immersed in 20 mL aqueous solution of $NaNO_3$ (2.3 M) under stirring overnight. In sequence, 2 mL of aqueous solution of HNO_3 (1 M HNO_3) was added and kept under constant stirring for approximately 2 h. Thus, such solutions were titrated with aqueous solution of $AgNO_3$ (0.0205 N) until the endpoint volume was identified. The IEC values of resulting AEMs were calculated by the volume of $AgNO_3$ solution that consumed the amount of the Cl^- through titration as shown in Equation 2 (Table 1).

Water uptake (WU) of AEM in the chloride form (3 × 3 cm) was calculated by using Equation 3 (Table 1), where m_{hyd} is the weight of wet membrane, and m_{dry} is the weight of dry membrane. Furthermore, in-plane swelling (IPS) and through-plane swelling (TPS) were estimated by using Equations 4 and 5 (Table 1), respectively, taking into account the area and thickness of both dry and wet for each sample. In all cases, the samples were soaked in UPW for 24 h at RT and wiping them in filter paper to eliminate water molecules not trapped inside the samples. The dry sample was measured after drying samples in a vacuum oven at 50 °C for 12 h. In addition, the WU, IPS, TPS, and hydration number (λ, Equation 6) were determined at different temperatures (40–80 °C) keeping the sample for 1 h for each temperature. All experiments of this section were done using n = 3 samples of each AEM.

Table 1
Summarizing equations used to determine membrane properties.

Characterization	Description	Equation
DoG	$DoG\ (\%) = \frac{m_g - m_i}{m_i} \times 100$ m_i = weight of the polymer before grafting step m_g = weight of the polymer after grafting step	**(1)**
IEC	$IEC\ (mmol/g) = \frac{V * F_c}{mdry}$ V = the volume of solution used Fc = 0.0205 N m_{dry} = dry weight of AEM	**(2)**
WU	$WU\ (\%) = \frac{m_{hyd} - m_{dry}}{m_{dry}} \times 100$ m_{hyd} = weight of wet membrane m_{dry} = weight of dry membrane	**(3)**
IPS	$IPS\ (\%) = \frac{A_{hyd} - A_{dry}}{A_{dry}} \times 100$ A_{wet} = area of wet membrane A_{dry} = area of dry membrane	**(4)**
TPS	$TPS\ (\%) = \frac{t_{hyd} - t_{dry}}{t_{dry}} \times 100$ t_{hyd} = thickness of wet membrane t_{dry} = thickness of dry membrane	**(5)**
λ	$\lambda = \frac{WU}{IEC\ x\ 18.02\ x\ 100}$ The value 18.02 refers to H_2O molar mass	**(6)**

2.7. Atomic force microscopy measurement

Atomic force microscopy (AFM) measurements were carried out using an Agilent 5500 AFM/SPM atomic force microscope. Prior to AFM measurements, the samples were dried at 50 °C for 12 h. The membrane surface topography images were obtained in soft tapping mode under room temperature and ambient atmospheric conditions. AFM images were acquired on each sample to determine mean roughness values and their associated standard deviations. The topographic parameters were evaluated in terms of average roughness (R_a), root mean square roughness (R_{MS}), and maximum height (H_m).

2.8. Electrochemical characterizations

2.8.1. Anion conductivity (σ)

Prior to the measurement, each sample (1 × 4 cm) was previously placed in an aqueous solution of KOH 1 M for 24 h, washed with UPW, and subsequently put in a 4-probe conductivity measurements apparatus (BT-112 conductivity cell, Scribner Associates). The measurements were conducted in the temperature range of 30–80 °C, with 100% of relative humidity (RH) under a constant N_2 (99.9992%) flow of 0.5 mL min^{-1}. A constant potential of 0.8 V was applied to generate a current between 800 and 1000 μA responsible for the rapid decarbonation of the sample for 3 h at 40 °C before the measurement started. After the decarbonation process, a scanning *dc* sweep from −0.1 V to 0.1 V was conducted using a potentiostat coupled to a Scribner Assoc. 850E fuel cell test station each 10 min, 4 times for each cell temperature. The resistance was obtained by the linear fit of the linear voltage-current data and the conductivity was calculated by using Equation (7) with d = 0.425 cm and "w" and "t" are the width and thickness of the hydrated AEM samples, respectively. All experiments in this section were done using n = 3 samples for each AEM. The methodology described can be consulted in detail elsewhere [35,36].

$$\sigma = \frac{d}{R\ x\ w\ x\ t} \qquad \text{Equation (7)}$$

2.8.2. Membrane electrode assembly (MEA) and fuel cell tests

Gas diffusion electrodes (GDE) were prepared for fuel cell and short-term durability tests. Pt/C (Alfa Aesar, Johnson Matthey HiSPEC 4000,

40% wt% Pt) was used as a catalyst in the cathode as well as PtRu/C (Alfa Aesar, Johnson Matthey HiSPEC 12100 40 wt% Pt and 20 wt% Ru) was used in the anode. The cathode catalyst ink was prepared by mixing Pt/C catalyst (80 wt% of the total solid mass) and homemade powdered anion-exchange ionomer (AEI) (20 wt% of the total solid mass) with 1 mL of water and 9 mL of propan-2-ol solvents. The anode catalyst ink was prepared by mixing PtRu/C catalyst (53 wt% of the total solid mass), AEI (20 wt% of the total solid mass), carbon Vulcan (27 wt% of the total solid mass) with 1 mL of water and 9 mL of propan-2-ol solvents. Previously to deposition, the ink was sonicated for 30 min at room temperature and sprayed over a paper gas diffusion substrate (Toray TGP-H-60 carbon paper, GDL Teflonated) by using a spray gun with nitrogen. The effective electrode area was 5 cm^2 and Pt loadings were 0.5 ± 0.03 mg cm^{-2} for both anode and cathode.

AEI-based on ETFE powder (Fluon® Z-8820X, AGC Europe), used as ionomer in the GDE, was pre-irradiated using e-beam radiation source in air, RT, and radiation absorbed dose of 100 kGy. Briefly, pre-irradiated ETFE powder (5 g) was immersed in aqueous solution containing 5% vol. VBC (Sigma-Aldrich, 97% purity, mixture of 3- and 4-isomers) and 1% vol. 1-octyl-2-pyrrolidone dispersant (Sigma-Aldrich). The powdered AEIs have an IEC of 2.30 ± 0.01 mmol g^{-1}. The detailed methodology for solid AEI synthesis is described elsewhere [37].

The electrodes and AEMs (4×4 cm) were immersed in an aqueous solution KOH (1 M) for 1 h to form AEM/AEI in OH^- form and then washed carefully with UPW to remove the excess of OH^-. The MEA was prepared by sandwiching the AEM between two freshly prepared electrodes, and it was assembled in single fuel cell hardware by applying a torque of 5.5 N m.

H_2/O_2 fed (CO_2-free) AEMFC tests were performed on 5 cm^2 single cell hardware (Scribner Assoc. USA). The fuel cell tests were conducted in a Scribner Assoc. 850E fuel cell station. The beginning-of-life polarization curves were taken in the galvanostatic mode at 60 °C, humidification temperature at 55 °C with gas supply of 1.0 L min^{-1} for both H_2 (99.999%) and O_2 (99.998%).

2.8.3. Stability tests

The chemical AEM stability tests were performed using the same protocol described in item 2.8.1. The tests were conducted accomplished at a fixed temperature of 80 °C, and relative humidity of 80%. The AEM conductivity data were collected at each 15 min for 100 h. The stability data were obtained from the normalized OH^- conductivity loss (% h^{-1}) as a function of time, after linear regression of the resulting data.

Short-term H_2/O_2 fed (CO_2-free) AEMFC tests were carried out by fixing a constant current to generate a voltage of 0.7 V for 100 h, and the fuel cell voltage loss was registered. The durability tests were conducted in a Scribner Assoc. 850E fuel cell station. The temperature of AEMFC was kept at 60 °C with H_2 (99.999%) anode gas flow = 0.5 L min^{-1}, and O_2 (99.998%) cathode gas flow = 0.5 L min^{-1}. The temperatures of the reacting gases were adjusted periodically during durability tests to ensure adequate membrane hydration (55 ± 2 °C). All measurements were repeated on three identical samples.

3. Results and discussion

3.1. Preparation and structure analysis of the RAFT-AEM

RIG-based AEM preparation involves three fundamental processes: i) irradiation, ii) grafting, and iii) functionalization. In the simultaneous RIG method, the free radicals are formed simultaneously on both the ETFE film and VBC. The radicals react to promote the grafting of VBC onto the film and homopolymerization of monomers in solution, with predominance of one to another, depending on reactional environments, such as reactants type and concentration, temperature as well as radiation atmosphere (inert or oxidative). The homopolymerization is an undesirable process in the production of AEMs, leading to the consumption of monomers that should be used in the grafting process. Moreover, the grafting process is responsible for the attachment of side chains in the base polymer, which in turn has the purpose of sustaining the functional groups responsible for ionic conduction. The irradiation, grafting, and quaternization form processes are represented in Scheme S1.

The general mechanism of RAFT polymerization was proposed in 1998 by the Common Wealth Scientific and Industrial Research Organization (CSIRO) [38]. The mechanism is based on the formation of free radical sites on polymer chains, which are available either initiating the polymerization, when in touch with a monomer, or recombining with other radicals. The initiation step occurs by the homolytic cleavage of the bond between molecules and atoms by the deposition of radiation energy leading to the creation of ions, excited species, and free radicals, then the radical formed can be added to another monomer to proceed with the chain reaction [38]. The grafts are grown as a result of their action of free radical sites formed onto a polymer base and monomers. On the other hand, the homopolymer can be formed in the RIG simultaneously method promoted by the reaction involving only monomer-free radical species. The high degree of grafting yields and low homopolymer contents are obtained if the polymer backbone is much more susceptive to grafting than the monomer to polymerize and/or if the concentration of the monomers is low [39]. As a sequence, the propagating radical is added to the RAFT agent and generates an intermediate radical, in which fragments form new radical and macro-RAFT agents (polymer chains bearing RAFT agent chain transfer moieties). The next step consists of the RAFT agent-formed radical restarting the polymerization by its reaction with monomer to form another propagating radical. The main reaction equilibrium is regarding active propagating groups and dormant polymeric RAFT agent-derived compounds reaction. The resulting products of RAFT polymerization are chains with or without thiocarbonylthio end-groups at the ω-end (living and dead chains, respectively) [18]. Scheme 1 summarizes the processes involved in the RAFT-based grafting of VBC onto ETFE through ionizing radiation.

The conventional-RIG and RAFT-based (ETFE-g-poly(VBC)) AEMs were submitted to the amination step, e.g., treatment of the ETFE-g-poly (VBC) films with trimethylamine, which converts the non-ionic films to covalently bond to QA head-groups (-NR_3), conferring to ETFE-g-poly (VBC) the ability to conduct anions such as Cl^-, HCO_3^-, and OH^- [40].

To elucidate the effect of the RAFT agent in the AEM structure, NMR experiments were conducted. Fig. S1 shows the $^{13}C\{^1H\}$ cross polarization under magic angle spinning (CP-MAS) spectra of the resulting AEMs with the band around 22 ppm, coming from the ETFE, used as a normalization parameter. The peaks at 119 and 22 ppm are attributed to the CF_2 and CH_2 of the ETFE, respectively. The peak at 119 ppm is strongly underestimated due to reduced magnetization transfer from protons. The peaks at 147 and 131 ppm are assigned to the aromatic carbons of the VBC monomer [41]. In addition, the peaks at 45 and 41 ppm are due to the CH_2 and CH_3 aliphatic carbons of the VBC, respectively. The peak at 53 ppm is attributed to the methylammonium carbons, whereas the peak at 69 ppm is related to the C–N carbons of TMA. The spectra confirm that all samples were synthesized successfully using the RAFT-RIG methodology. The peak area data are compiled and can be better visualized in Table S1.

The CP-MAS experiments, as performed, could not provide an absolute quantitative analysis, however, a comparison between spectra of the samples with respect to the ETFE peak intensities gives information about the tendency in forming homopolymer. Notably, the NMR spectra (see Fig. S1) show that the peak intensities referred to VBC decrease as the quantities of RAFT agent increase in the homopolymerization reaction i.e., from E0 to E30 (also noticeable in the peak area listed in Table S1). Such a feature confirms the suppression of the grafting reaction with the increasing amount of RAFT agent in good agreement with DoG data.

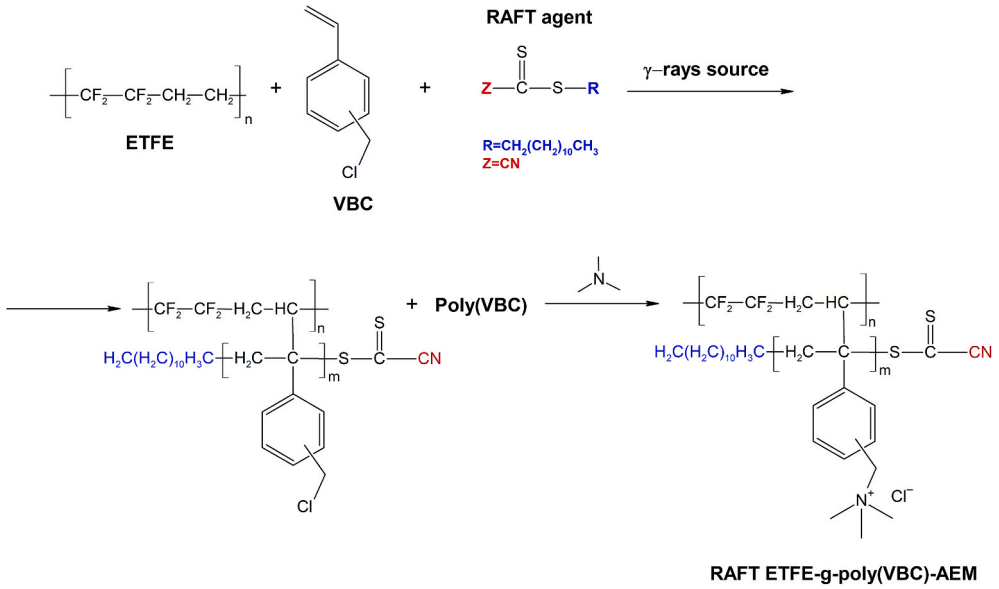

Scheme 1. Preparation of ETFE-g-poly(VBC) membranes by the RAFT polymerization and amination with TMA.

3.2. Membrane properties

Properties, such as degree of grafting, ion-exchange capacity, water uptake, through and in-plane swelling, and hydration number of all AEMs are summarized in Table 2. In terms of DoG, a decrease in the values as the amount of RAFT agent increases is evidenced. This is entirely consistent with the hypothesis that the incorporation of RAFT agent reduces the degree of grafting by controlling side chain molecular size during the grafting process once the RAFT agent is bound to the monomer to promote the VBC copolymerization [29]. However, it does not, necessarily, reflect a decrease in VBC grafting, mainly, if considers a significant diminishing in the AEM molecular weight, which can likely hide true DoG values estimated by gravimetric measurement.

In general, IEC tends to increase proportionally with DoG once the ion transport capacity is directly related to the number of functional groups attached to the side chains produced by grafting [42]. Nonetheless, it was observed that IEC values decrease slightly with the increase of RAFT agent during the grafting process, not following the proportionality observed for DoG variation. Practically, there is no IEC variation evidence for E0 (non-RAFT agent) and E5 (RAFT = 5 mg) with IEC values of 2.32 mmol g^{-1}. On the other hand, more appreciable difference is observed for E15 (RAFT = 15 mg) and E30 (RAFT = 30 mg) AEMs with IEC values of 2.10 and 1.90 mmol g^{-1}, respectively. Such differences represent a decrease of about 18% in IECs and 62% in DoG values when comparing AEMs non-RAFT agent with those obtained with the highest amount of RAFT agent (E30). Therefore, the evidence of a proportional difference between the DoG and IEC values for E0 and E30 reinforces that DoG and IEC follow a decreasing trend with the increase in the amount of RAFT agent. This observation suggests an underestimation in the absolute values of the DoG of the RAFT-AEMs due to a reduction in the size of the side chain.

The WU of the AEM are properties closely associated with the quantity of QA in the molecular structure of the membrane [43,44]. Water absorption is a very important parameter for AEMs, and is responsible for their main electrochemical characteristics, but it must be controlled since affects their dimensional stability and mechanical properties. WU values presented in Table 2 follow the trend E0 ≈ E5 > E15 > E30, which means that WU decreases as the RAFT agent amount increases. It is worth noting that WU follows both DoG and IEC. The DoG decreasing as a function of RAFT agent amount is likely a result of the suppression effect of the grafting reaction in RAFT-AEM, affecting the QA number and, consequently, the IEC. In addition, the hydration number (λ) follows the same trend observed for WU, indicating that the RAFT agent suppresses water absorption, but without affecting the ionic conductivity in the same proportion, since other effects such as the AEM microstructure, which can be influenced by the RAFT agent, are also important properties in the conduction mechanisms.

Excessive WU and swelling properties affect the dimensional stability of AEMs. Consequently, variations in swelling states can trigger membrane detachment between electrodes within the MEA, resulting in poor AEMFC performance [45]. The dimensional swelling variation in the area is associated with IPS as well as the thickness variation under wet and dry states is ascribed as TPS (Table 2). IPS values are notably influenced by humidity levels, which in turn aligns with IEC. Despite this, TPS (Table 2) is practically unaltered for all AEMs. Indeed, TPS values exhibit a modest thickness variation (~18%) at room temperature. On the other hand, for temperatures as high as 80 °C, the TPS values demonstrate more pronounced changes. For instance, the E0 sample experiences an increase from 17% at RT to 53% in TPS at 80 °C, while for E5, E15 and E30 samples, TPS varies from 17% to 48%; 18%–47%, and 18%–40%, respectively. Thus, at higher temperatures, TPS is in line with IEC values, as shown in Fig. S4. Moreover, it is worth mentioning that not only TPS, but also other water-related parameters, such as WU, IPS, and λ, increase with the temperature increase (see Figs. S3, S5, and S6).

Gel permeation chromatography (GPC) was used to measure the molecular weight and evaluate the influence of the RAFT agent on the grafting process (Fig. 1). In contrast to E0, which presents a bimodal

Table 2
Degree of grafting (DoG), ion-exchange capacity (IEC), water uptake (WU), through-plane (TPS), and in-plane swelling (IPS), hydration number (λ) for RIG-AEM (E0) and RAFT-based AEM synthesized with different amounts of RAFT agent (E5, E15, and E30).

AEM Properties	E0	E5	E15	E30
Ratio (Monomer/RAFT)	1065	540	181	91
DoG (%)	102 ± 3	84 ± 1	69 ± 1	63 ± 3
IEC (mmol g^{-1})	2.36 ± 0.03	2.32 ± 0.03	2.10 ± 0.02	1.90 ± 0.01
WU (%)	59 ± 2	55 ± 1	42 ± 1	21 ± 2
IPS (%)	21 ± 2	20 ± 2	13 ± 3	9 ± 3
TPS (%)	17 ± 1	17 ± 2	18 ± 1	18 ± 1
λ	14 ± 2	13 ± 2	11 ± 1	6 ± 2

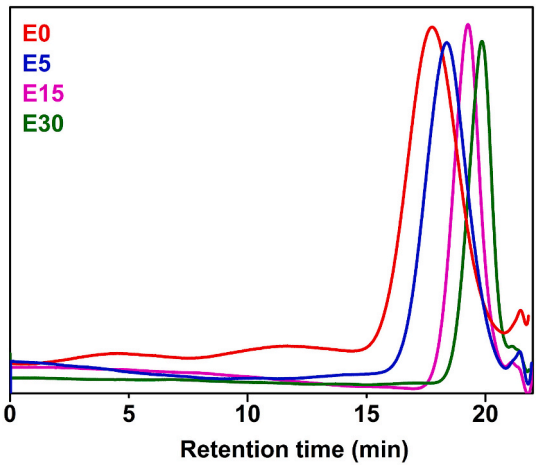

Fig. 1. Gel permeation chromatography chromatograms of E0 (red line), E5 (blue line), E15 (magenta line), and E30 (green line). (For interpretation of the references to colour in this figure legend, the reader is referred to the Web version of this article.)

profile, the elution behavior in the GPC experiments for solutions of RAFT-based AEM is essentially unimodal, indicating an excellent uniformity of chains. The average molecular weight ($\overline{M}_W$) was found to decrease remarkably as a function of the increasing amount of RAFT. The $\overline{M}_W$ values of 29.608; 17.381; 6.773 and 3.674 g mol^{-1} were obtained for E0, E5, E15, E30, respectively. Similarly, the dispersity index ($\overline{M}_W/\ \overline{M}_n$, where $\overline{M}_n$ is the number averaged molecular weight) was calculated to be 2.8, 2.8, 2.2, and 1.7, respectively to E0, E5, E15, and E30. This indicates a narrower and more uniform M_W distribution for RAFT-based AEMs in comparison to conventional RIG-AEMs. This finding suggests that the monomer polymerization is strongly controlled by the RAFT agent, with a peak of about 15–20.5 min corresponding to the homopolymer in solution, which is in excellent agreement with the literature [29]. Chen and Seko [46] also observed a decrease in both parameters molecular weight and dispersion in poly(CMS) grafted onto ETFE films after the addition of RAFT agent. In addition, the authors reported that a higher concentration of RAFT agents in the monomer solution could effectively trap the radicals generated by irradiation. Then, this approach can be used for producing monodispersed polymers or oligomers for specific applications.

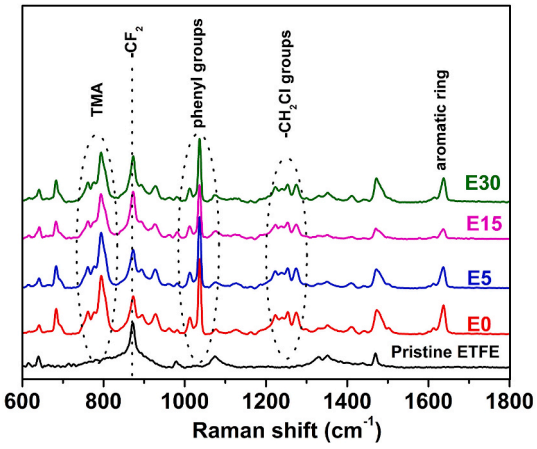

Fig. 2. Raman spectra of pristine ETFE film (black line), E0 (red line), E5 (blue line), E15 (magenta line) and E30 (green line). The data were collected using an excitation wavelength of 785 nm and laser power of 85 mW. (For interpretation of the references to colour in this figure legend, the reader is referred to the Web version of this article.)

Fig. 2 shows the Raman spectra of pristine ETFE and resulting AEMs. For pristine ETFE, intense bands at 870 cm^{-1} attributable to CF_2 stretches and at 1400 cm^{-1} associated with CH_2 bonds confirm the inherent perfluorinated character of ETFE [47]. For AEMs, a band at 1035 cm^{-1} assigned to the ring-breathing vibrations of phenyl units was evidenced for all membranes. The bands at 1200 and 1630 cm^{-1} corresponding to –CH_2Cl groups and aromatic ring vibration, respectively, were observed indicating the successful grafting in the presence of RAFT agent [47,48]. A small band centered at 756 cm^{-1} was ascribed to the amination due to the presence of the quaternary ammonium group (-$N^+(CH_3)_3$). A band at 780 cm^{-1} referring to C–S stretching vibration of the RAFT chain-end groups of the grafted VBC it was not detected. The same was reported by Çelik et al. [29] indicating that the high-intensity bands of ETFE backbone and graft-saturated absorbed bands in this region cause overlay on RAFT groups in the Raman signal.

3.3. Thermal properties

Thermal stability is a crucial factor for AEMs to be considered in fuel cells. Thermal stability was evaluated using TGA and DSC techniques. Fig. 3 shows the TGA/DTG curves obtained in a temperature range from 25 °C to 650 °C under N_2 atmosphere. These conditions are consistent with the decomposition processes of polymeric backbone, side chains (copolymers), and functional groups in conventional RIG-AEM (E0) and RAFT-AEMs (E5, E15 and E30). All membranes exhibit different steps of weight loss thermal degradation around 100 °C, 200–300 °C, 350–450 °C, and above 500 °C. The first weight loss (100 °C) is related to the desorption of water bonded to the anionic group, mainly the water-sensitive portion of the AEM associated with functional groups (hydrophilic clusters), followed by the decomposition process of such functional groups (200–300 °C) [48]. A third step (350–450 °C) can be attributed to the thermal degradation of side chains of poly (VBC)-grafted to ETFE, and the last thermal degradation has been assigned to the ETFE polymer backbone degradation [49]. In terms of temperature, no shift in the processes is evidenced for RAFT-AEMs, indicating that the thermal degradation processes are essentially unaltered. However, by analyzing TGA data, it is possible to observe that RAFT-AEMs have significantly lower mass loss (E0 = 7%; E5 = 6%; E15 = 12%; E30 = 5%) in the third step (side chain degradation) compared to AEM grafted without RAFT agent. This is an indication that the thermal stability is not affected by the ordering of chains effect caused by the RAFT agent in the AEMs grafts structure, as all samples started to lose weight around 180 °C, attributed to the functional groups.

The DSC curves are presented in Fig. S2. An endothermic peak at about 263 °C was evidenced for all the membranes, indicating that the observed T_m is independent of both RAFT agent amount and RIG conditions. Considering that the T_m is directly related to the intrinsic

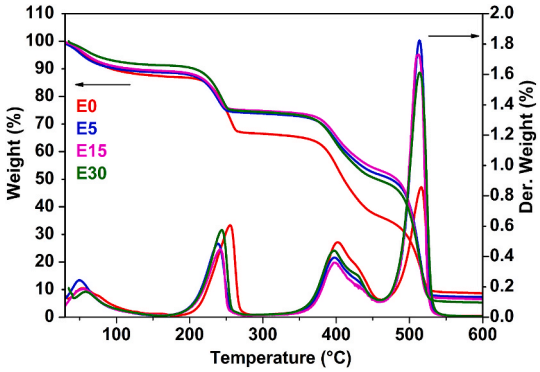

Fig. 3. TGA (left axis) and DTG (right axis) curves of all AEMs. E0 (red line), E5 (blue line), E15 (magenta line), and E30 (green line). (For interpretation of the references to colour in this figure legend, the reader is referred to the Web version of this article.)

properties of the base polymer, it is possible to infer that the RAFT does not influence significantly the thermal properties of the samples. In Figs. S2–b, it is possible to identify exothermic peaks between 234 and 238 °C, which were ascribed as the crystallization temperature (T_c) of samples. No appreciable shift on the T_c is evidenced for RAFT-AEMs, revealing that the RAFT agent has no influence on the crystallization transition of the polymer. Such a finding is reasonable once the RAFT acts in the copolymerization step, associated with side chain growth, while the crystallization process is primarily associated with the polymer backbone. The results reveal that the thermal processes of the proposed AEMs follow the same trend of the respective ETFE backbone. Furthermore, the values presented are in agreement with the literature for pristine ETFE and other similar materials based on ETFE [29,50–53].

3.4. Mechanical properties

The mechanical properties of AEMs were evaluated by uniaxial tensile stress tests and the main results are summarized in Table 3. In order to avoid operational errors, each sample was measured using three specimens and the results presented represent the average of these measurements. All AEMs exhibited the standard profile of stress increases as a function of strain percentage. Moreover, a higher Young's modulus and tensile strength hand elongation at break were observed for E5, E15, and E30 in comparison to E0 samples.

Young's modulus is an indirect measurement of the stiffness of the polymer given by the ratio between stress and strain. In AEM, any change in Young's modulus is associated with the amount of monomer grafted to the polymer matrix, which is primarily responsible for its mechanical characteristics. This parameter is measured in the early portion of the curve. Moreover, Young's modulus is higher for RAFT-AEMs in comparison to E0, having a linear growth with the amount of RAFT agent. In terms of Young's modulus values, E0 and E5 are quite similar while E15 and E30 showed a fourfold increase in this property.

Analyzing the elongation at break and tensile strength results, it can be observed that both elastic modulus and tensile strength increase significantly in RAFT-AEMs in comparison to conventional grafted AEM. This confirms an enhancement in the stiffening property, which in turn can be related to the decrease in IPS and WU for RAFT-AEMs. According to the literature, water molecules cause a plastic effect on the membrane that can be responsible for reducing the mechanical properties of the membrane [54,55]. Moreover, polymers partially fluorinated as ETFE trends to form less chain scission after the irradiation process, as a consequence the polymers presented higher molecular weight and improvement of properties such as strength break and toughness [56]. Thus, by increasing the addition of RAFT it was possible to observe the same contribution of this agent on mechanical properties. According to the literature stress at break, elongation at break, and Young's modulus should be > 10, $> 100\%$, and between 75 and 400 MPa, respectively as being required for fuel cell membranes [12].

Fig. 4 shows the profile of the tensile stress-strain of AEMs, where two important points are observed: i) the resilience increases with the RAFT agent content, suggesting that the material can absorb energy without suffering damage; ii) the fracture points, which can be related to the modulus of toughness, are remarkable high for RAFT-AEMs, indicating good impact resistance. Thus, both parameters are an indicator that the RAFT agent contributes remarkably positive to the mechanical reinforcement of AEMs.

Table 3
Tensile strength, Young's modulus, and elongation at break results of all AEMs.

AEM properties	E0	E5	E15	E30
Tensile strength (MPa)	14 ± 5	22 ± 1	25 ± 1	21 ± 3
Young's modulus (MPa)	253 ± 20	275 ± 15	408 ± 9	418 ± 25
Elongation at break (%)	130 ± 30	190 ± 6	189 ± 8	220 ± 19

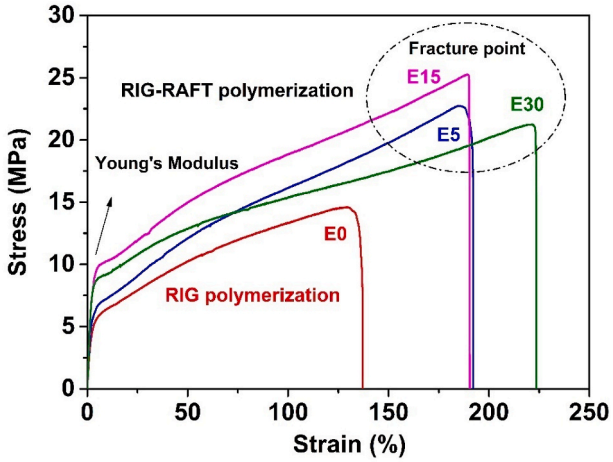

Fig. 4. The tensile stress-stain curves at room temperature for E0 (red line), E5 (blue line), E15 (magenta line), and E30 (green line) AEMs in the chloride form. (For interpretation of the references to colour in this figure legend, the reader is referred to the Web version of this article.)

3.5. Membrane morphology

Fig. 5 depicts the topographic images of the grafting process evolution for pristine ETFE (a), and E0 (b), E5 (c), E15 (d), E30 (e) AEMs obtained by AFM analysis. The AFM images illustrate that the introduction of poly(VBC) into the ETFE film is capable of changin the surface roughness (9.0 nm) for all AEMs, while ETFE film exhibits several many spiked projections (see Fig. S7). Fig. 5b–e shows how the surface topography of AEMs evolves from the introduction of grafted side chains in conventional RIG-AEM (Fig. 5-b) to RAFT-based AEM with different RAFT contents (Fig. 5c–e). The surface roughness was 24.0 nm, 18.9 nm, 15.7 nm, and 10.9 nm for E0, E5, E15 and E30, respectively. These results reveal that RAFT-based AEMs present significant differences in the surface roughness compared with conventional RIG-AEM (E0), probably resulting from morphological modification of AEMs in the presence of RAFT agent.

In terms of the morphology of the AEMs, the dark regions are related to the hydrophilic domains containing the QAs, and the bright regions to the hydrophobic domains composed by the ETFE backbone, in which alternating arrangement of bright and dark regions suggests the phase separation morphology of the AEM [57–59]. Morphology control is a fundamental parameter for enhancing the AEM properties such as ion conductivity, stability, and AEMFC performance [57–59]. By comparing conventional RIG-AEMs and RAFT-based AEMs (E5, E15, and E30), it is possible to notice that E0 and E15 present a poor uniformity morphology as well as E5 and E30 exhibit a more ordered morphology. This finding indicates a well-balanced spatial arrangement for E5 and E30 in comparison to E0 and E15, suggesting that the improvement in dimensional, mechanical and chemical stabilities can be associated with the more ordered morphology as a result of the side chain length control introduced by RAFT agent.

3.6. Conductivity measurement

The high ionic conductivity (σ) associated with thermal, mechanical, and chemical stability are requirements for using AEMs application in electrochemical devices. However, reconciling all these properties in one membrane has been truly challenging. In order to evaluate whether the presence of RAFT can affect the anion conductivity, not by the amount of QA, but by a controlled arrangement of the side chains in the AEM structure. By considering that in the grafting process involving RAFT agent, the side chains have a more consistent and controlled chain length, it is expected that the ionic conduction mechanism would be also

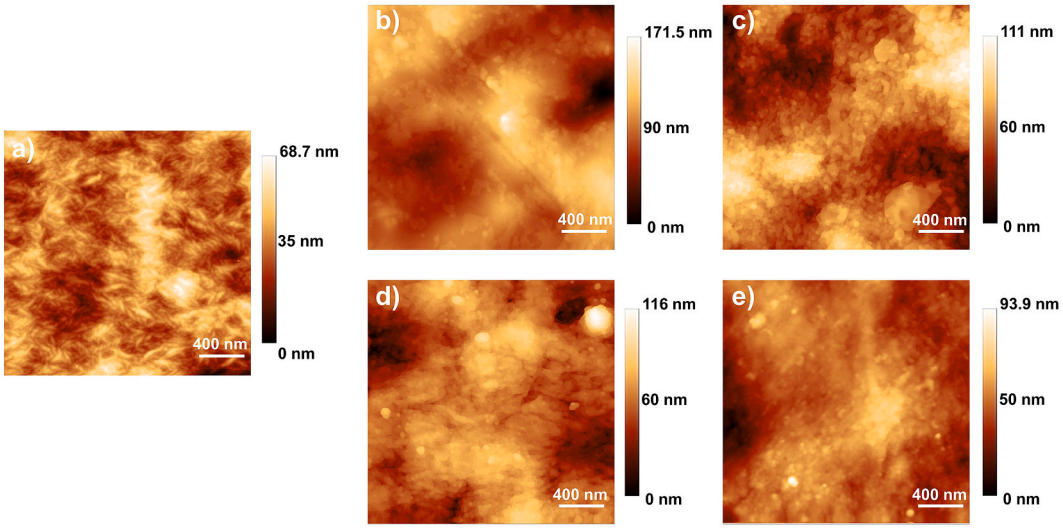

Fig. 5. AFM images with 400 nm-scale resolution for pristine ETFE film (a), and E0 (b), E5 (c), E15 (d), E30 (e) AEMs in the chloride form.

facilitated. In general, the mechanism of ionic conductivity in AEMs is dependent on the characteristics related to the water absorption of the AEM, in which the mechanism is governed by a combination of vehicular diffusion and Grøtthuss mechanism through the water network, contributing to the water content balance in the AEM [60–63].

The "true hydroxide conductivity" of the membrane was determined by following the procedure described by Dekel et al. [35,36], where a constant voltage is applied continuously to generate a current that avoids the carbonation process of AEM. Fig. 6 presents the σ profile as a function of the temperature (30–80 °C). The conductivity values are ranging from 99 to 244 mS cm^{-1} (30–80 °C) irrespective of the presence of the RAFT agent. For example, the values at 80 °C were 244, 236, 217, and 235 mS cm^{-1}, corresponding to E0, E5, E15, and E30 AEMs, respectively. Such conductivities values are close to those previously found in our group [64] and significantly superior to their conductivity values for another ETFE-based AEMs produced by conventional RIG (see Table S3).

Fig. 6 shows that σ does not follow the IEC for the E30 sample. Specifically at 80 °C, the σ for E30 is similar to that of samples E0 and E5, and even superior to that for E15. It is notable that the IEC value of the E30 samples is comparatively lower in relation to the other samples: E0 (2.36) ≈ E5 (2.32) > E15 (2.10) > E30 (1.90). A priori, this fact is not intuitive since the water absorption in AEMs, in general, is proportional to the IEC. Hossain et al. [45] demonstrated that AEMs with comparable IEC might exhibit different conductivities due to their morphological structures. Moreover, Dang et al. [65] report that differences in OH^- conductivity among AEMs with approximately 25% variation in IEC and similar λ could be attributed to their molecular architectures. The authors hypothesized that the length of the side chain plays a role in promoting ionic clustering and phase separation, ultimately leading to enhanced mobility of side chains within AEMs.

In this context, AFM analysis (Fig. 5) demonstrated that RAFT-AEM exhibits a more ordered morphology in comparison to conventional RIG-AEM (E0), which contributed to significant differences in the roughness of RAFT-AEMs. Particularly for E5 and E30, hydrophilic/hydrophobic phase separation is more evident, which could indicate an increase in the local concentration of OH^- ions within the aggregated domains. Hence, these findings could support for confirming that conductivity is not only associated with IEC but also with the arrangement of ionic domains in the structural morphology of AEMs. Furthermore, this can explain the main differences in the disparities between IEC and conductivity in RAFT-based AEMs, where the morphology is directly affected by the manipulation of side chain length.

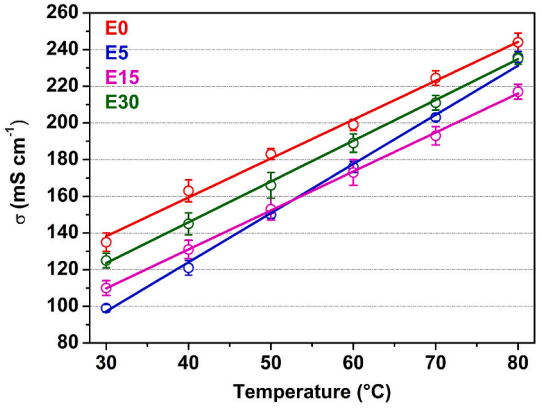

Fig. 6. The conductivity dependence with temperature, The "true Hydroxide conductivity" of E0 (red line), E5 (blue line), E15 (magenta line), and E30 (green line) between 30 and 80 °C and RH = 100%. (In some points, the standard deviation bars are very small and they appear overlapping or inside the data circles). (For interpretation of the references to colour in this figure legend, the reader is referred to the Web version of this article.)

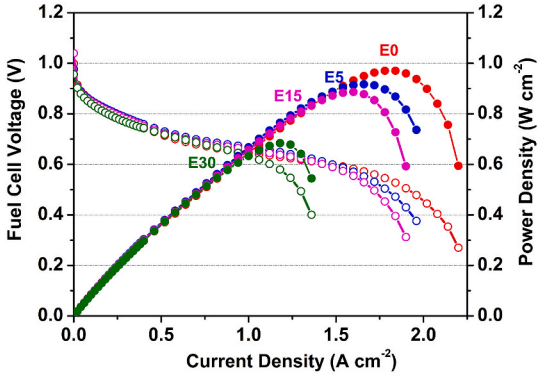

Fig. 7. AEMFCs performances at 60 °C with H_2 anode gas flow = 1.0 L min^{-1}, and O_2 cathode gas flow = 1.0 L min^{-1}, both supplied unpressurized with optimal dew-point temperatures of 55 °C. Catalysts: PtRu/C at the anodes and Pt/C at the cathodes. Pt loadings of 0.5 ± 0.03 mg cm^{-2}. The thickness AEMs in the OH^- form were 69 μm (E0), 63 μm (E5), 61 μm (E15), 55 μm (E30).

3.7. AEMFC performance

Fig. 7 shows beginning-of-life H_2/O_2 AEMFC polarization and respective power density curves for RIG-AEM (E0) and RAFT-AEMs (E5, E15, E30) operating at 60 °C. A typical polarization profile for AEMFC is evidenced for all the membranes characterized by the activation, ohmic drop and mass transfer overpotentials. The overpotential activation observed at low current densities region (up to 0.3 A cm^{-2}) is resultant of the electronic transfer associated with the slow kinetics of the reactions involved in the electrodes as a rate-determining step, which is essentially attributed to oxygen reduction reaction (ORR). The second relevant overpotential is related to ohmic drop, evidenced in intermediate current densities (up to 1.3 A cm^{-2}), which is primarily caused by losses in conducting components, such as membranes, bipolar plates, and electrodes. Taking into account that electrodes and bipolar plates are composed of conducting materials, the ohmic drop overpotential can be essentially associated with the conductance response of AEMs. Finally, the mass transfer overpotential refers to the diffusion of reactants - resulting from the difference between the rates of consumption of reactant and formation of product - as the rate-determining step [66,67].

In terms of performance, the maximum power density for E0, E5, E15, and E30 samples were 0.97, 0.92, 0.88, and 0.68 W cm^{-2} at 60 °C, respectively, following the same IEC trend: E0 (2.36) ≈ E5 (2.32) > E15 (2.10) > E30 (1.90). Analyzing the polarization curves, it can be noted that the ohmic drop overpotential is quite similar for the different AEMs as previously discussed. The main difference in polarization response, and consequently in the power density curves, is a result of the mass transport overpotential, which can be observed by the limiting current density values, ranging from 2.2 to 1.4 A cm^{-2} for E0 to E30 samples, respectively.

Such a feature can be related to the complex water management attributed to an unbalance in the water movement between anode and cathode electrodes [68]. Several factors impact the water management within the fuel cell, including gas flow, dew-point, fuel cell temperature, gas diffusion layer, ionomer composition in the catalyst layer, and the inherent morphology of the membrane [69–72]. The AEM can facilitate the liquid water from the anode to the cathode depending on the movement of water within its structure. Then, the lowest power density for E30 should be mostly associated with the WU. In fact, E30 sample showed WU of 52% at 60 °C (see Fig. S4), while WU for E0, E5 and E15 samples were 90%, 75%, and 70%, respectively. In turn, water absorption behavior in E30 can be a result of the low roughness, i.e. more compact morphology, characteristic of this sample. Comparing E0, E5 and E15 no appreciable difference in maximum power density was identified, suggesting that the low content of RAFT agent in the AEM structure does not affect significantly the net AEMFC performance.

3.8. Stability tests

Fig. 8 shows the short-term alkaline stability tests for conventional RIG-AEM and RAFT-AEMs obtained at 80 °C, RH = 80% during 100 h. The results are presented as a normalization of the conductivity value as a function of time, where the rate (% h^{-1}) is the normalized conductivity loss determined by a linear fitting. The data show the following trend in stability: E5 > E30 > E0 > E15. E5 and E30 samples have the lowest conductivity losses, 0.05 and 0.09% h^{-1}, respectively, while E0 and E15 have a conductivity loss of approximately 0.15% h^{-1}. In this case, there is an improvement in the stability of 160% when comparing the E0 and E5 samples. The superior chemical stability for E5 and E30 can be a result of better-ordered morphology as previously discussed and confirmed by AFM results. Furthermore, such results are comparable to or better than those found in the literature for similar RIG-AEM based on ETFE [32,60,73] or other polymer backbones (see Table S3). These findings have been supported by literature as evidence that composition and structure control are possible way to get around the degradation

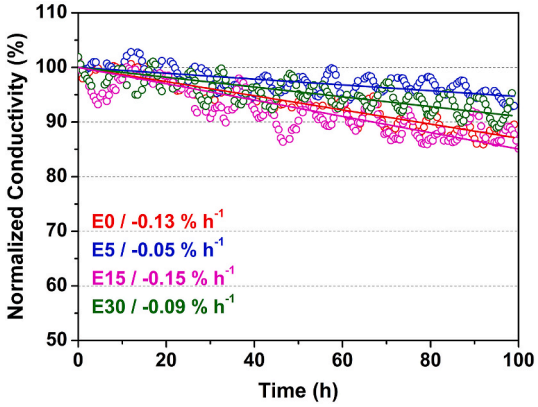

Fig. 8. Normalized conductivity loss at 80 °C, RH = 80% for E0 (red line), E5 (blue line), E15 (magenta line), and E30 (green line) AEMs in the OH^- form during 100 h. (For interpretation of the references to colour in this figure legend, the reader is referred to the Web version of this article.)

effects of AEMs resulting from the processing.

Han et al. [74] reported a reduced susceptibility to attacks by OH^- ions inthe backbone of AEMs with well-ordered phase separation morphology. Thereby, the authors suggest that the chemical stability is enhanced when the membrane micromorphology is well-defined, contributing to low IPS and WU as well as the hydroxide ions must be better located in the hydrophilic domains. In addition, Long and Pivovar [75] explain in a very elegant way that the preferential route of degradation of alkyltrimethylammonium groups in AEMs is the Hoffman elimination. However, the steric effect caused by the increase of the QA side chain (2–4 carbon atoms), improved the stability of the studied membranes, nevertheless, there is an ideal spacing limit between backbone and QA that must be considered (4–6 carbon atoms). This occurs due to the existing mutual inductive effect between the QA and the backbone of some types of AEMs, but it is minimized due to the distance increase. The elongation of the side chains has been reported as a possible relationship with the improvement of AEMs stability [75,76]. The same approach can be applied to RAFT-AEMs, which means that elongated side chains arranged in an ordered structure can protect the QA groups from nucleophilic attacks caused by OH^- ions. Indeed, it is evident that besides the elongation of the side chains, the ordering of the polymer chains can lead to the improvement of the stability of AEMs [75–77].

Finally, short-term H_2/O_2 AEMFC durability tests for E0 and E5 AEMs are shown in Fig. S8. Figs. S8–a shows that the fuel cell voltage loss for E0 and E5 samples in the initial hours of the test is significantly different. For the initial 10 h, E0 has a degradation ratio of 1.8 mV h^{-1}, while for E5 this value was close to 0.6 mV h^{-1}. After 50 h the differences between the samples remain evident, and E0 has 5 mV h^{-1} while E5 has 2 mV h^{-1}. After 60 h the fuel cell voltage loss is equivalent for both samples. It is noteworthy that this type of durability test, i.e., performance in a single fuel cell, takes into account all aspects of degradation processes in AEMFC, such as its components and operating conditions, which makes it difficult to separate the effective and isolated contribution of the membrane for durability. Such a feature is evidenced in polarization curves obtained before (beginning-of-life) and after (end-of-life) durability tests (Figs. S8–b). The beginning-of-life polarization curves for both E0 and E5 present similar polarization profiles, indicating very similar MEAs. A slight difference is observed at higher current densities or in the region of the diffusion-limiting overpotential, which is very sensitive to humidification conditions, but in the case of short-term durability testing at 0.7 V, no significant irreversible loss is expected. On the other hand, the end-of-life polarization curves reveal an appreciable performance loss for both E0 and E5, caused more remarkably by higher activation overpotential, which is mostly related

to the electrode.

It is important to mention that the catalyst layers are composed of a solid ionomer without binder addition, which can lead to leaching of this component during the durability test, resulting in progressive both electrode activity and ionic conductivity losses in the triple-phase boundary, consistent with higher activation and ohmic drop over-potentials observed in end-of-time curves. Obviously, it is not possible to attribute the loss of performance exclusively to the ionomer, but under these conditions, it seems to be the predominant factor. More appreciable performance loss is evidenced for E0, which is in good agreement with true OH- stability experiments and reinforces the higher stability found for RAFT-based AEMs.

Taking into account the literature approaches, the results obtained in this work show that, in addition to the backbone nature, QA type, and synthesis methodology, microstructure control plays an important role in the stability profile of AEMs. As a result, structural control of AEMs may be an option for achieving a balance of performance and stability in AEMFCs.

4. Conclusions

In this work, it was presented a series of anion-exchange membranes based on ETFE with well-ordering molecular structure using a reversible addition-fragmentation chain transfer agent combined with radiation-induced grafting. The strategy described here represents a promising practical route towards the rational design of the next generation of AEMs for application in fuel cells. The incorporation of the RAFT agent in the synthetic route enabled membranes with reduced water uptake behavior, as well as good dimensional stability, excellent mechanical strength, and good thermal stability. Moreover, the experimental results demonstrated that the RAFT-AEMs obtained can have hydroxide conductivity comparable to a standard AEM and, consequently, the same trend was observed for AEMFC performance, showing that the new design can enhance the electrochemical properties through well-ordered conductive channels. Certainly, the key result presented here was about the excellent chemical stability of RAFT-AEM compared to the standard AEM. The stability tests showed that the E5 sample has the lowest conductivity loss (0.05% h^{-1}) being 160% higher than the E0 sample (0.13% h^{-1}). AFM images indicate a well-balanced spatial arrangement for E5 and E30 in comparison to E0 and E15, suggesting that the improvement in dimensional, mechanical and chemical stabilities can be associated with the well-ordered morphology as a result of the side chain length control introduced by RAFT agent. Finally, it can be concluded that the use of the RAFT agent not only improved the AEM properties and fuel cell performance, but also enhanced the chemical stability, and this is considered the most important target to be developed in AEMFCs.

Author contributions

Bianca Pedroso S. Santos - Conceptualization, Data curation, Investigation, Methodology, Visualization, Writing – Original draft, Writing – Review & editing. **Andrey S. Barbosa** - Conceptualization, Data curation, Investigation, Methodology, Visualization, Writing – Original draft, Writing – Review & editing. **Yasko Kodama** - Conceptualization, Investigation, Methodology, Writing – Original draft, Writing – Review & editing. **Thiago B. de Queiroz:** Data curation, Methodology, Writing – Review & editing. **Elisabete I. Santiago**: Conceptualization, Funding acquisition, Project administration, Resources, Supervision, Writing – Original draft, Writing – Review; editing.

Declaration of competing interest

The authors declare that they have no known competing financial interests or personal relationships that could have appeared to influence the work reported in this paper.

Data availability

Data will be made available on request.

Acknowledgements

This work was financially supported by the *Center for Innovation on New Energies* (CINE) - SHELL (ANP)/FAPESP grant No. 2017/11937–4, FAPESP 2020/13466-1, CNPq SisH2 407967/2022–2, the Brazilian Nuclear Energy Commission (CNEN), and International Atomic Energy Agency, research project contract: IAEA RC 23708. The authors are grateful to UFABC Multiuser Central Facility for access to NMR and AFM equipment, to Prof. Dr. Alexandre J. C. Lanfredi for analysis, support and discussion about AFM measure, to Prof. Dr. Jean Jacques Bonvent for support with AFM measure, to Prof. Dr. Marcos Lopes Dias of IMA/UFRJ for support and analysis of GPC measure, to Eng. Elizabeth S. Somessari for the irradiation of the ETFE films, and to MSc. Djalma Batista Dias for the support with mechanical tests, both performed at Radiation Technology Center - CETER-IPEN, and to Dr. Ana Laura G. Biancolli for support and discussion about AEMFC durability tests. Prof. Dr. Elisabete Inácio Santiago is a fellow of the Brazilian CNPq.

Appendix A. Supplementary data

Supplementary data to this article can be found online at https://doi.org/10.1016/j.memsci.2023.122071.

References

[1] D.R. Dekel, Review of cell performance in anion exchange membrane fuel cells, J. Power Sources 375 (2018) 158–169, https://doi.org/10.1016/j.jpowsour.2017.07.117.
[2] A. Treshchalov, A. Kikas, V. Kisand, J. Aruv, Transition Metal (Fe, Co, Mn, Cu) Containing Nitrogen-Doped Porous Carbon as Efficient Oxygen Reduction Electrocatalysts for Anion Exchange Membrane Fuel Cells, 2023, p. 458, https://doi.org/10.1016/j.cej.2023.141468.
[3] M.M. Hossen, M.S. Hasan, M.R.I. Sardar, J. bin Haider, Mottakin, K. Tammeveski, P. Atanassov, State-of-the-art and developmental trends in platinum group metal-free cathode catalyst for anion exchange membrane fuel cell (AEMFC), Appl. Catal. B Environ. (2022), 121733, https://doi.org/10.1016/j.apcatb.2022.121733.
[4] W. You, K.J.T. Noonan, G.W. Coates, Alkaline-stable anion exchange membranes: a review of synthetic approaches, Prog. Polym. Sci. 100 (2020), 101177, https://doi.org/10.1016/j.progpolymsci.2019.101177.
[5] N. Chen, Y.M. Lee, Anion exchange polyelectrolytes for membranes and ionomers, Prog. Polym. Sci. 113 (2021), 101345, https://doi.org/10.1016/j.progpolymsci.2020.101345.
[6] J. Huang, Z. Yu, J. Tang, P. Wang, Q. Tan, J. Wang, X. Lei, A review on anion exchange membranes for fuel cells: anion-exchange polyelectrolytes and synthesis strategies, Int. J. Hydrogen Energy 47 (2022) 27800–27820, https://doi.org/10.1016/j.ijhydene.2022.06.140.
[7] A.S. Barbosa, A.L.G. Biancolli, A.J.C. Lanfredi O R Jr., F.C. Fonseca, E.I. Santiago, Enhancing the durability and performance of radiation-induced grafted low-density polyethylene-based anion-exchange membranes by controlling irradiation conditions, J. Membr. Sci. 659 (2022), 120804, https://doi.org/10.2139/ssrn.4120345.
[8] A.W. Tricker, J.K. Lee, J.R. Shin, N. Danilovic, A.Z. Weber, Design and operating principles for high-performing anion exchange membrane water electrolyzers, J. Power Sources 567 (2023), 232967, https://doi.org/10.1016/j.jpowsour.2023.232967.
[9] M.T. Tsehaye, X. Yang, T. Janoschka, M.D. Hager, U.S. Schubert, E. Planes, F. Alloin, C. Iojoiu, Anion exchange membranes with high power density and energy efficiency for aqueous organic redox flow batteries, Electrochim. Acta 438 (2023), 141565, https://doi.org/10.1016/j.electacta.2022.141565.
[10] M.I. Khan, A. Shanableh, S.M. Osman, M.H. Lashari, S. Manzoor, A. ur Rehman, R. Luque, Fabrication of trimethylphosphine-functionalized anion exchange membranes for desalination application via electrodialysis process, Chemosphere 308 (2022), 136330, https://doi.org/10.1016/j.chemosphere.2022.136330.
[11] M. Hren, M. Božič, D. Fakin, K.S. Kleinschek, S. Gorgieva, Alkaline membrane fuel cells: anion exchange membranes and fuels, Sustain. Energy Fuels 5 (2021) 604–637, https://doi.org/10.1039/d0se01373k.
[12] L. Wang, J.J. Brink, Y. Liu, A.M. Herring, J. Ponce-González, D.K. Whelligan, J. R. Varcoe, Non-fluorinated pre-irradiation-grafted (peroxidated) LDPE-based anion-exchange membranes with high performance and stability, Energy Environ. Sci. 10 (2017) 2154–2167, https://doi.org/10.1039/c7ee02053h.
[13] M.M. Nasef, E.S.A. Hegazy, Preparation and applications of ion exchange membranes by radiation-induced graft copolymerization of polar monomers onto

non-polar films, Prog. Polym. Sci. 29 (2004) 499–561, https://doi.org/10.1016/j.progpolymsci.2004.01.003.
[14] G. Couture, A. Alaaeddine, F. Boschet, B. Ameduri, Polymeric materials as anion-exchange membranes for alkaline fuel cells, Prog. Polym. Sci. 36 (2011) 1521–1557, https://doi.org/10.1016/j.progpolymsci.2011.04.004.
[15] M.M. Nasef, Radiation grafted ion conducting membranes for electrochemical energy systems: status of developmental and upscaled membranes, J. Appl. Membr. Sci. Technol. 26 (2022) 51–76, https://doi.org/10.11113/amst.v26n1.233.
[16] M. Semsarilar, S. Perrier, "Green" reversible addition-fragmentation chain-transfer (RAFT) polymerization, Nat. Chem. 2 (2010) 811–820, https://doi.org/10.1038/nchem.853.
[17] J. Tanaka, N.E. Archer, M.J. Grant, W. You, Reversible-addition fragmentation chain transfer step-growth polymerization, J. Am. Chem. Soc. 143 (2021) 15918–15923, https://doi.org/10.1021/jacs.1c07553.
[18] S. Perrier, 50th anniversary perspective: RAFT polymerization - a user guide, Macromolecules 50 (2017) 7433–7447, https://doi.org/10.1021/acs.macromol.7b00767.
[19] Y. Kodama, M. Barsbay, O. Güven, Radiation-induced and RAFT-mediated grafting of poly(hydroxyethyl methacrylate) (PHEMA) from cellulose surfaces, Radiat. Phys. Chem. 94 (2014) 98–104, https://doi.org/10.1016/j.radphyschem.2013.07.016.
[20] T. Masuda, M. Takai, Structure and properties of thermoresponsive gels formed by RAFT polymerization: effect of the RAFT agent content, Polym. J. 52 (2020) 1407–1412, https://doi.org/10.1038/s41428-020-00401-x.
[21] C. Dommanget, F. D'Agosto, V. Monteil, Polymerization of ethylene through reversible addition-fragmentation chain transfer (RAFT), Angew. Chem. Int. Ed. 53 (2014) 6683–6686, https://doi.org/10.1002/anie.201403491.
[22] C. Fu, Z. Huang, C.J. Hawker, G. Moad, J. Xu, C. Boyer, RAFT-mediated, visible light-initiated single unit monomer insertion and its application in the synthesis of sequence-defined polymers, Polym. Chem. 8 (2017) 4637–4643, https://doi.org/10.1039/c7py00713b.
[23] C.M.R. Abreu, P. Maximiano, T. Guliashvili, J. Nicolas, A.C. Serra, J.F.J. Coelho, Cyclopentyl methyl ether as a green solvent for reversible-addition fragmentation chain transfer and nitroxide-mediated polymerizations, RSC Adv. 6 (2016) 7495–7503, https://doi.org/10.1039/c5ra21975b.
[24] Z. Sun, B. Choi, A. Feng, G. Moad, S.H. Thang, Nonmigratory poly(vinyl chloride)-block-polycaprolactone plasticizers and compatibilizers prepared by sequential RAFT and ring-opening polymerization (RAFT-T-ROP), Macromolecules 52 (2019) 1746–1756, https://doi.org/10.1021/acs.macromol.8b02146.
[25] H.S. Wang, N.P. Truong, Z. Pei, M.L. Coote, A. Anastasaki, Reversing RAFT polymerization: near-quantitative monomer generation via a catalyst-free depolymerization approach, J. Am. Chem. Soc. 144 (2022) 4678–4684, https://doi.org/10.1021/jacs.2c00963.
[26] R. Koyilapu, S. Subhadarshini, S. Singha, T. Jana, An in-situ RAFT polymerization technique for the preparation of poly(N-vinyl imidazole) modified Cloisite nanoclay to develop nanocomposite PEM, Polymer (Guildf) 212 (2021), 123175, https://doi.org/10.1016/j.polymer.2020.123175.
[27] N. Mukherjee, A. Das, M. Dhara, T. Jana, Surface initiated RAFT polymerization to synthesize N-heterocyclic block copolymer grafted silica nanofillers for improving PEM properties, Polymer (Guildf) 236 (2021), 124315, https://doi.org/10.1016/j.polymer.2021.124315.
[28] Q. Ge, G. Wang, X. Zhu, W. Yu, J. Zhou, B. Wu, Y. Liu, Z. Zheng, Z. Yang, J. Qian, A highly stable aliphatic backbone from visible light-induced RAFT polymerization for anion exchange membranes, Polym. Chem. 12 (2021) 5574–5582, https://doi.org/10.1039/d1py00867f.
[29] G. Çelik, M. Barsbay, O. Güven, Polymer Chemistry towards New Proton Exchange Membrane Materials with Enhanced Performance via RAFT, 2015, https://doi.org/10.1039/c5py01527h.
[30] T. Tran Duy, S. ichi Sawada, S. Hasegawa, Y. Katsumura, Y. Maekawa, Poly (ethylene-co-tetrafluoroethylene) (ETFE)-based graft-type polymer electrolyte membranes with different ion exchange capacities: relative humidity dependence for fuel cell applications, J. Membr. Sci. 447 (2013) 19–25, https://doi.org/10.1016/j.memsci.2013.07.041.
[31] J. Ponce-González, I. Ouachan, J.R. Varcoe, D.K. Whelligan, Radiation-induced grafting of a butyl-spacer styrenic monomer onto ETFE: the synthesis of the most alkali stable radiation-grafted anion-exchange membrane to date, J. Mater. Chem. A 6 (2018) 823–827, https://doi.org/10.1039/c7ta10222d.
[32] S. Willdorf-Cohen, A. Zhegur-Khais, J. Ponce-González, S. Bsoul-Haj, J.R. Varcoe, C.E. Diesendruck, D.R. Dekel, Alkaline stability of anion-exchange membranes, ACS Appl. Energy Mater. (2022), https://doi.org/10.1021/acsaem.2c03689.
[33] A.E. Bennett, C.M. Rienstra, M. Auger, K.V. Lakshmi, R.G. Griffin, A.E. Bennett, C. M. Rienstra, R.G. Griffin, Heteronuclear Decoupling in Rotating Solids Heteronuclear Decoupling in Rotating Solids, 1995, p. 6951, https://doi.org/10.1063/1.470372.
[34] D. Massiot, F. Fayon, M. Capron, I. King, S. Le Calvé, B. Alonso, J.O. Durand, B. Bujoli, Z. Gan, G. Hoatson, Modelling one- and two-dimensional solid-state NMR spectra, Magn. Reson. Chem. 40 (2002) 70–76, https://doi.org/10.1002/mrc.984.
[35] A. Zhegur-Khais, F. Kubannek, U. Krewer, D.R. Dekel, Measuring the true hydroxide conductivity of anion exchange membranes, J. Membr. Sci. 612 (2020), 118461, https://doi.org/10.1016/j.memsci.2020.118461.
[36] J. Müller, A. Zhegur, U. Krewer, J.R. Varcoe, D.R. Dekel, Practical ex-situ technique to measure the chemical stability of anion-exchange membranes under conditions simulating the fuel cell environment, ACS Mater. Lett. 2 (2020) 168–173, https://doi.org/10.1021/acsmaterialslett.9b00418.
[37] A.L.G. Biancolli, D. Herranz, L. Wang, G. Stehlíková, R. Bance-Soualhi, J. Ponce-González, P. Ocón, E.A. Ticianelli, D.K. Whelligan, J.R. Varcoe, E.I. Santiago, ETFE-based anion-exchange membrane ionomer powders for alkaline membrane fuel cells: a first performance comparison of head-group chemistry, J. Mater. Chem. A 6 (2018) 24330–24341, https://doi.org/10.1039/c8ta08309f.
[38] M. Barsbay, O. Güven, A short review of radiation-induced raft-mediated graft copolymerization: a powerful combination for modifying the surface properties of polymers in a controlled manner, Radiat. Phys. Chem. 78 (2009) 1054–1059, https://doi.org/10.1016/j.radphyschem.2009.06.022.
[39] M.M. Nasef, H. Saidi, A.M. Dessouki, E.M. El-Nesr, Radiation-induced grafting of styrene onto poly(tetrafluoroethylene) (PTFE) films. I. Effect of grafting conditions and properties of the grafted films, Polym. Int. 49 (2000) 399–406, https://doi.org/10.1002/(SICI)1097-0126(200004).
[40] R. Bance-Soualhi, M. Choolaei, S.A. Franklin, T.R. Willson, J. Lee, D.K. Whelligan, C. Crean, J.R. Varcoe, Radiation-grafted anion-exchange membranes for reverse electrodialysis: a comparison of N,N,N′,N′-tetramethylhexane-1,6-diamine crosslinking (amination stage) and divinylbenzene crosslinking (grafting stage), J. Mater. Chem. A 9 (2021) 22025–22038, https://doi.org/10.1039/d1ta05166k.
[41] J.R. Varcoe, R.C.T. Slade, E. Lam How Yee, S.D. Poynton, D.J. Driscoll, D. C. Apperley, Poly(ethylene-co-tetrafluoroethylene)-derived radiation-grafted anion-exchange membrane with properties specifically tailored for application in metal-cation-free alkaline polymer electrolyte fuel cells, Chem. Mater. 19 (2007) 2686–2693, https://doi.org/10.1021/cm062407u.
[42] J. Chen, M. Asano, T. Yamaki, M. Yoshida, Preparation of sulfonated crosslinked PTFE-graft-poly(alkyl vinyl ether) membranes for polymer electrolyte membrane fuel cells by radiation processing, J. Membr. Sci. 256 (2005) 38–45, https://doi.org/10.1016/j.memsci.2005.02.005.
[43] Z.Y. Zhu, W.W. Gou, J.H. Chen, Q.G. Zhang, A.M. Zhu, Q.L. Liu, Crosslinked naphthalene-based triblock polymer anion exchange membranes for fuel cells, J. Membr. Sci. 636 (2021), 119569, https://doi.org/10.1016/j.memsci.2021.119569.
[44] X. Zhou, L. Wu, G. Zhang, R. Li, X. Hu, X. Chang, Y. Shen, L. Liu, N. Li, Rational design of comb-shaped poly(arylene indole piperidinium) to enhance hydroxide ion transport for H_2/O_2 fuel cell, J. Membr. Sci. 631 (2021), https://doi.org/10.1016/j.memsci.2021.119335.
[45] M.M. Hossain, J. Hou, L. Wu, Q. Ge, X. Liang, A.N. Mondal, T. Xu, Anion exchange membranes with clusters of alkyl ammonium group for mitigating water swelling but not ionic conductivity, J. Membr. Sci. 550 (2018) 101–109, https://doi.org/10.1016/j.memsci.2017.12.062.
[46] J. Chen, N. Seko, Effects of RAFT agent on the chloromethylstyrene polymerizations in a simultaneous radiation grafting system, Polymers (Basel) 9 (2017), https://doi.org/10.3390/polym9080307.
[47] W.H. Lee, C. Crean, J.R. Varcoe, R. Bance-Soualhi, A Raman spectro-microscopic investigation of ETFE-based radiation-grafted anion-exchange membranes, RSC Adv. 7 (2017) 47726–47737, https://doi.org/10.1039/c7ra09650j.
[48] J. Ponce-González, D.K. Whelligan, L. Wang, R. Bance-Soualhi, Y. Wang, Y. Peng, H. Peng, D.C. Apperley, H.N. Sarode, T.P. Pandey, A.G. Divekar, S. Seifert, A. M. Herring, L. Zhuang, J.R. Varcoe, High performance aliphatic-heterocyclic benzyl-quaternary ammonium radiation-grafted anion-exchange membranes, Energy Environ. Sci. 9 (2016) 3724–3735, https://doi.org/10.1039/c6ee01958g.
[49] J. Fang, Y. Yang, X. Lu, M. Ye, W. Li, Y. Zhang, Cross-linked, ETFE-derived and radiation grafted membranes for anion exchange membrane fuel cell applications, Int. J. Hydrogen Energy 37 (2012) 594–602, https://doi.org/10.1016/j.ijhydene.2011.09.112.
[50] Y. Huang, D.F. Miranda, C. Iacob, S. Zhang, Y. Dan, J. Runt, Crystalline microstructure and dielectric properties of oriented poly (ethylene-co-tetra fl uoroethylene), Polymer 113 (2017) 1–8, https://doi.org/10.1016/j.polymer.2017.02.038.
[51] N.S. Kwak, J.S. Koo, T.S. Hwang, Synthesis and characterization of EFFE-g-(VBTAC-co-HEMA) anion exchange membranes prepared by a ^{60}Co radiation-induced graft copolymerization for redox-flow battery applications, Macromol. Res. 20 (2012) 205–211, https://doi.org/10.1007/s13233-012-0032-3.
[52] J. Feng, C. Chan, Compatibility and Properties of Alternating Ethylene-Tetrafluoroethy Lene Copolymer and Poly (Methyl Methacrylate) Blends, vol. 38, 1997, pp. 6371–6378.
[53] J.M. Song, S.Y. Lee, H.S. Woo, J.Y. Sohn, J. Shin, Thermal behavior of poly (vinylbenzyl chloride)-grafted poly(ethylene-co- tetrafluoroethylene) films, J. Polym. Sci., Part B: Polym. Phys. 52 (2014) 517–525, https://doi.org/10.1002/polb.23445.
[54] A.N. Lai, D. Guo, C.X. Lin, Q.G. Zhang, A.M. Zhu, M.L. Ye, Q.L. Liu, Enhanced performance of anion exchange membranes via crosslinking of ion cluster regions for fuel cells, J. Power Sources 327 (2016) 56–66, https://doi.org/10.1016/j.jpowsour.2016.07.043.
[55] R. Espiritu, M. Mamlouk, K. Scott, Study on the effect of the degree of grafting on the performance of polyethylene-based anion exchange membrane for fuel cell application, Int. J. Hydrogen Energy 41 (2016) 1120–1133, https://doi.org/10.1016/j.ijhydene.2015.10.108.
[56] H. Ben Youcef, S.A. Gürsel, A. Buisson, L. Gubler, A. Wokaun, G.G. Scherer, Influence of radiation-induced grafting process onmechanical properties of ETFE-based membranes for fuel cells, Fuel Cell. 10 (2010) 401–410, https://doi.org/10.1002/fuce.200900200.
[57] M. Zhu, X. Zhang, Y. Wang, Y. Wu, H. Wang, M. Zhang, Q. Chen, Z. Shen, N. Li, Novel anion exchange membranes based on quaternized diblock copolystyrene containing a fluorinated hydrophobic block, J. Membr. Sci. 554 (2018) 264–273, https://doi.org/10.1016/j.memsci.2018.01.055.
[58] W. Song, K. Peng, W. Xu, X. Liu, H. Zhang, X. Liang, B. Ye, H. Zhang, Z. Yang, L. Wu, X. Ge, T. Xu, Upscaled production of an ultramicroporous anion-exchange

membrane enables long-term operation in electrochemical energy devices, Nat. Commun. 14 (2023), https://doi.org/10.1038/s41467-023-38350-7.
[59] Y. Pan, K. Jiang, X. Sun, S. Ma, Y.M. So, H. Ma, X. Yan, N. Zhang, G. He, Facilitating ionic conduction for anion exchange membrane via employing star-shaped block copolymer, J. Membr. Sci. 630 (2021), 119290, https://doi.org/10.1016/j.memsci.2021.119290.
[60] K.N. Grew, W.K.S. Chiu, A dusty fluid model for predicting hydroxyl anion conductivity in alkaline anion exchange membranes, J. Electrochem. Soc. 157 (2010) B327, https://doi.org/10.1149/1.3273200.
[61] C. Chen, Y.L.S. Tse, G.E. Lindberg, C. Knight, G.A. Voth, Hydroxide solvation and transport in anion exchange membranes, J. Am. Chem. Soc. 138 (2016) 991–1000, https://doi.org/10.1021/jacs.5b11951.
[62] V. Dubey, A. Maiti, S. Daschakraborty, Predicting the solvation structure and vehicular di ff usion of hydroxide ion in an anion exchange membrane using nonreactive molecular dynamics simulation, Chem. Phys. Lett. 755 (2020), 137802, https://doi.org/10.1016/j.cplett.2020.137802.
[63] D. Dong, W. Zhang, A.C.T. Van Duin, D. Bedrov, Grotthuss versus Vehicular Transport of Hydroxide in Anion- Exchange Membranes: Insight from Combined Reactive and Nonreactive Molecular Simulations, 2018, https://doi.org/10.1021/acs.jpclett.8b00004.
[64] A.L.G. Biancolli, S. Bsoul-Haj, J.C. Douglin, A.S. Barbosa, R.R. de Sousa, O. Rodrigues, A.J.C. Lanfredi, D.R. Dekel, E.I. Santiago, High-performance radiation grafted anion-exchange membranes for fuel cell applications: effects of irradiation conditions on ETFE-based membranes properties, J. Membr. Sci. 641 (2022), https://doi.org/10.1016/j.memsci.2021.119879.
[65] H.S. Dang, E.A. Weiber, P. Jannasch, Poly(phenylene oxide) functionalized with quaternary ammonium groups via flexible alkyl spacers for high-performance anion exchange membranes, J. Mater. Chem. A 3 (2015) 5280–5284, https://doi.org/10.1039/c5ta00350d.
[66] H.-S. Shiau, I.V. Zenyuk, A.Z. Weber, Elucidating performance limitations in alkaline-exchange- membrane fuel cells, J. Electrochem. Soc. 164 (2017), https://doi.org/10.1149/2.0531711jes. E3583–E3591.
[67] K. Yassin, I.G. Rasin, S. Brandon, D.R. Dekel, Quantifying the critical effect of water diffusivity in anion exchange membranes for fuel cell applications, J. Membr. Sci. 608 (2020), 118206, https://doi.org/10.1016/j.memsci.2020.118206.
[68] W.E. Mustain, M. Chatenet, M. Page, Y.S. Kim, Durability challenges of anion exchange membrane fuel cells, Energy Environ. Sci. 13 (2020) 2805–2838, https://doi.org/10.1039/d0ee01133a.
[69] C.E. Diesendruck, D.R. Dekel, Water – a key parameter in the stability of anion exchange membrane fuel cells, Curr. Opin. Electrochem. 9 (2018) 173–178, https://doi.org/10.1016/j.coelec.2018.03.019.
[70] T.J. Omasta, L. Wang, X. Peng, C.A. Lewis, J.R. Varcoe, W.E. Mustain, Importance of balancing membrane and electrode water in anion exchange membrane fuel cells, J. Power Sources 375 (2018) 205–213, https://doi.org/10.1016/j.jpowsour.2017.05.006.
[71] S. Gottesfeld, D.R. Dekel, M. Page, C. Bae, Y. Yan, P. Zelenay, Y.S. Kim, Anion exchange membrane fuel cells: current status and remaining challenges, J. Power Sources 375 (2018) 170–184, https://doi.org/10.1016/j.jpowsour.2017.08.010.
[72] W.E. Mustain, Understanding how high-performance anion exchange membrane fuel cells were achieved: component, interfacial, and cell-level factors, Curr. Opin. Electrochem. 12 (2018) 233–239, https://doi.org/10.1016/j.coelec.2018.11.010.
[73] S. Haj-Bsoul, J.R. Varcoe, D.R. Dekel, Measuring the alkaline stability of anion-exchange membranes, J. Electroanal. Chem. 908 (2022), https://doi.org/10.1016/j.jelechem.2022.116112.
[74] J. Han, J. Pan, C. Chen, L. Wei, Y. Wang, Q. Pan, N. Zhao, B. Xie, L. Xiao, J. Lu, L. Zhuang, Effect of micromorphology on alkaline polymer electrolyte stability, ACS Appl. Mater. Interfaces 11 (2019) 469–477, https://doi.org/10.1021/acsami.8b09481.
[75] H. Long, B.S. Pivovar, Hydroxide degradation pathways for substituted benzyltrimethyl ammonium: a DFT study, ECS Electrochem. Lett. 4 (2015), https://doi.org/10.1149/2.0041501eel. F13–F16.
[76] L. Wang, M.A. Hickner, Highly conductive side chain block copolymer anion exchange membranes, Soft Matter 12 (2016) 5359–5371, https://doi.org/10.1039/c6sm00398b.
[77] C. Fujimoto, D.S. Kim, M. Hibbs, D. Wrobleski, Y.S. Kim, Backbone stability of quaternized polyaromatics for alkaline membrane fuel cells, J. Membr. Sci. 423–424 (2012) 438–449, https://doi.org/10.1016/j.memsci.2012.08.045.